Acta Pharmaceutica Sinica B 2025;15(2):1159−1170

Chinese Pharmaceutical Association
Institute of Materia Medica, Chinese Academy of Medical Sciences

Acta Pharmaceutica Sinica B

www.elsevier.com/locate/apsb
www.sciencedirect.com

ORIGINAL ARTICLE

NIR-II-activated whole-cell vaccine with ultra-efficient semiconducting diradical oligomers for breast carcinoma growth and metastasis inhibition

Yijian Gao[a,†], Yachao Zhang[b,d,†], Yujie Ma[a], Xiliang Li[a], Yu Wang[a], Huan Chen[c], Yingpeng Wan[a], Zhongming Huang[a], Weimin Liu[e,f], Pengfei Wang[e,f], Lidai Wang[d,*], Chun-Sing Lee[c,*], Shengliang Li[a,*]

[a]*College of Pharmaceutical Sciences, the Fourth Affiliated Hospital of Soochow University, Suzhou Medical College, Soochow University, Suzhou 215123, China*
[b]*Key Laboratory of Biomedical Imaging Science and System, Suzhou Institute of Biomedical Engineering and Technology, Chinese Academy of Sciences, Suzhou 215163, China*
[c]*Center of Super-Diamond and Advanced Films (COSDAF), Department of Chemistry, City University of Hong Kong, Hong Kong SAR 999077, China*
[d]*Department of Biomedical Engineering, City University of Hong Kong, Hong Kong SAR, China*
[e]*Technical Institute of Physics and Chemistry, Chinese Academy of Sciences, Beijing 100190, China*
[f]*Joint Laboratory of Nano-organic Functional Materials and Devices (TIPC and CityU), City University of Hong Kong, Hong Kong SAR 999077, China*

Received 4 July 2024; received in revised form 20 September 2024; accepted 15 October 2024

KEY WORDS

NIR-II;
Semiconducting oligomer;
Photothermal therapy;
Vaccine;
Nanoparticles;
Theranostics;

Abstract High-performance phototheranostics with combined photothermal therapy and photoacoustic imaging have been considered promising approaches for efficient cancer diagnosis and treatment. However, developing phototheranostic materials with efficient photothermal conversion efficiency (PCE), especially over the second near-infrared window (NIR-II, 1000−1700 nm), remains challenging. Herein, we report an ultraefficient NIR-II-activated nanomedicine with phototheranostic and vaccination capability for highly efficient *in vivo* tumor elimination and metastasis inhibition. The NIR-II nanomedicine of a semiconducting biradical oligomer with a motor-flexible design was demonstrated with a record-breaking PCE of 87% upon

---

*Corresponding authors.

E-mail addresses: lidawang@cityu.edu.hk (Lidai Wang), apcslee@cityu.edu.hk (Chun-Sing Lee), lishengliang@suda.edu.cn (Shengliang Li).

[†] These authors made equal contributions to this work.

Peer review under the responsibility of Chinese Pharmaceutical Association and Institute of Materia Medica, Chinese Academy of Medical Sciences.

https://doi.org/10.1016/j.apsb.2024.12.017

Breast carcinoma;
Immunotherapy

NIR-II excitation. This nanomedicine inherently features extraordinary photothermal stability, good biocompatibility, and excellent photoacoustic performance, contributing to high-contrast photoacoustic imaging in living mice and high-performance photothermal elimination of tumors. Moreover, a whole-cell vaccine based on a NIR-II nanomedicine with NIR-II-activated performance was further designed to remotely activate the antitumor immunologic memory and effectively inhibit tumor occurrence and metastasis *in vivo*, with good biosafety. Thus, this work paves a new avenue for designing NIR-II active semiconducting biradical materials as a promising theranostics platform and further promotes the development of NIR-II nanomedicine for personalized cancer treatment.

1. Introduction

Cancer vaccines have widely been considered a powerful approach for tumor prevention and suppression, in which the host innate immune system of the patient is actively activated to fight cancer cells[1-3]. In 2010, the US Food and Drug Administration (FDA) regularly permitted a dendritic cell (DC) vaccine for the treatment of drug-resistant prostate cancer and thus further promoted dramatic advances in cancer vaccines[4-6]. In recent years, many cancer vaccines, mainly including cell-relative and mRNA vaccines, have been explored, and their efficiency in tumor inhibition has been demonstrated[7,8]. However, most of these vaccines have relatively low responsibilities, which are generally lower than 15%. Moreover, antigen heterogeneity seriously restricts the further application of these materials in the clinic[5,9]. To overcome this limitation, recent efforts have concentrated on the design and exploitation of efficient personal vaccines, especially whole-cell vaccines. Whole-cell vaccines simultaneously provide abundant antigens for activating innate immunity against specific tumors in individual patients and greatly prevent boresome immune escape of the tumor[7,10-12]. It is thus critical to explore new whole-cell vaccines with efficient and controlled activities to satisfy the pressing needs for cancer treatment.

Photothermal therapy (PTT) employs light-absorbing materials to locally promote photon-to-thermal conversion from photoenergy and results in thermal ablation of the tumor[13-22]. In this approach, tumor cells actively generate and release potential antigens and signaling molecules associated with the immune response, which provides a promising opportunity to harness the host immune system of patients[23,24]. Many photothermal agents (PTAs), such as plasmonic nanostructures[25-27], 2D graphene and analogues[28-30], MXenes[31,32], organic dyes[33-35], and conjugated polymers[36-40], have demonstrated high performance in cancer therapy during the past few decades. Among the extant PTAs, near-infrared (NIR)-absorbing organic materials (including small molecules and polymers) have shadowed inorganic materials owing to their good biodegradability, inherent nontoxicity, and flexible processability[41-46]. In particular, their tunable optical absorption ranges enrich the photothermic feasibility, which fully endows PTT with practical superiority as an advanced therapeutic. To date, most efforts have concentrated on the development of organic PTAs activated with photons from the first NIR (NIR-I) window (700−1000 nm), which seriously restricted their applications in deep tissue[47-50]. The second NIR (NIR-II) window (1000−1700 nm) exhibits many appealing advantages for practical PTT over NIR-I[51-53]. These include less photon scattering, higher penetration depth, and larger maximum permissible exposure (MPE) (*e.g.*, the MPE at 1064 nm is 1 W/cm^2, whereas the MPE at 808 nm is only 0.33 W/cm^2) [54-56]. Thus, NIR-II PTT holds great promise for overcoming limitations that hinder the applications of PTAs[57-59]. However, investigations of NIR-II photothermal performance are rare because of the scarcity of high-performance NIR-II active organic PTAs. Recently, many studies have explored inorganic nanomaterials and conjugated polymers and demonstrated their advantages in NIR-II PTT[60-62]. However, the photothermal conversion efficiencies (PCEs) of the reported PTAs are still far below those of PTAs activated by NIR-I light[63,64]. To achieve high penetration depth and minimum phototoxicity, it is important to develop NIR-II PTAs with improved PCEs.

In this work, we designed and synthesized a NIR-II active semiconducting biradical oligomer TBS with a D-π-A-π-D architecture (bottom left of Fig. 1). TBS is equipped with motor-flexible and strong electron-withdrawing groups to offer strong absorption over the NIR-II window and highly efficient non-radiative transition. Water-dispersible nanoparticles (NPs) were fabricated *via* the self-assembly of TBS with amphiphilic polymers. It was shown that these NPs have a high PCE of 87% upon excitation with a 1064 nm light. Furthermore, the TBS NPs also showed good photoacoustic performance under NIR-II excitation, enabling promising *in vitro* and *in vivo* NIR-II photothermic tumor treatment as well as non-invasive photoacoustic imaging. Moreover, a whole-cell vaccine based on TBS NPs named NIR-II NV with NIR-II-activated performance was further designed to activate the antitumor immunological memory and effectively inhibit tumor occurrence and metastasis *in vivo*. This report offers a simple and promising approach to explore NIR-II-activated tumor vaccines and thus may enrich the development of NIR-II nanomedicine for personalized cancer treatment.

2. Materials and methods

2.1. Materials

All chemicals and agents were purchased from commercial manufacturers and used without further purification. 4,7-Dibromobenzo[1,2-*c*:4,5-*c*′]bis([1,2,5]thiadiazole) and 4,8-dibromo[1,2,5]selenadiazolo[3,4-*f*]benzo[*c*][1,2,5]thiadiazole were purchased from Derthon Optoelectronic Materials Science (Shenzhen, China). 1,2-Distearoyl-*sn*-glycero-3-phosphoethanolamine-*N*-[methoxy(polyethylene glycol)-2000] (DSPE-PEG$_{2000}$) were obtained from Yare Biological Technology Co., Ltd. (Shanghai, China). DSPE-PEG2K-PEI800 were obtained from Ruixi Biological Technology Co., Ltd. (Xi’an, China). DMEM culturing media and Calcein-acetoxymethyl

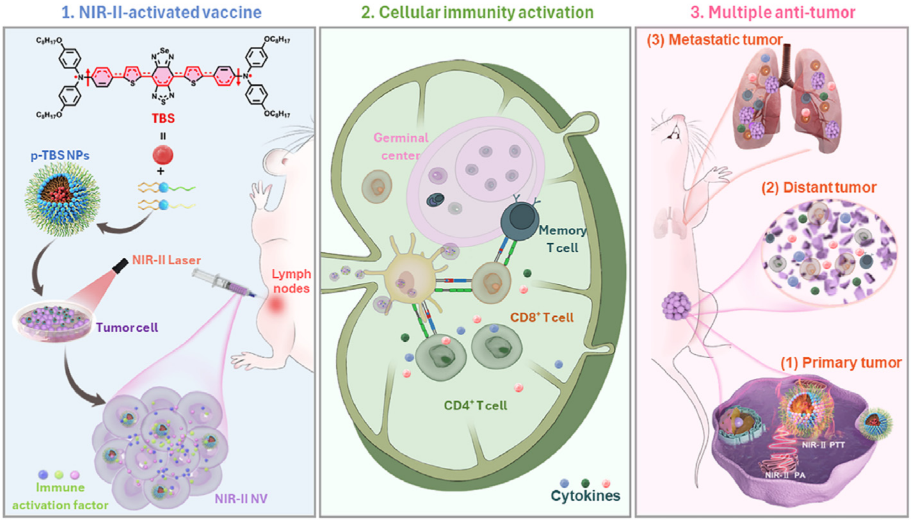

Figure 1 Diagrammatic drawing of NIR-II-activated photo theranostics and vaccines with semiconducting biradical oligomers.

ester (Calcein AM)/propidium iodide (PI) cell live/dead assay kit (catalog: CA1630) were purchased from Solarbio Life Sciences Co., Ltd. (Beijing, China). Fetal bovine serum (FBS) was purchased from Viva Cell (Shanghai, China). PE/Cyanine7 anti-mouse CD4 (catalog: 116016) and APC/Cyanine7 anti-mouse CD8a (catalog: 100714) antibodies were all purchased from BioLegend, Inc. (San Diego, USA). ELISA kits for TNF-α, IFN-γ, and IL-6 assay were all purchased from Aimeng Youning (Shanghai, China).

2.2. *Methods*

^{1}H and ^{13}C NMR spectra were recorded with Bruker Avance 600 MHz spectrometers. Mass spectra (MS) were performed using a 4800 Plus MALDI TOF/TOF Analyzer. The UV−Vis−NIR absorption spectra were recorded with a PerkinElmer Lambda 750 spectrophotometer. Morphology and size of NPs were performed on transmission electron microscopy (TEM, JEM-2010F, Hitachi). Dynamic light scattering (DLS) was recorded with a Malvern ZetaSizer Nano ZS90 system. The temperature variation and thermal images were precisely recorded with a thermal imaging camera from FLUKE technology. Cell fluorescence images were captured with a confocal laser scanning microscopy (A1R HD25, Nikon). Density functional theory (DFT) calculation was performed by the B3LYP/6G(d), Gaussian 09 package.

2.3. *Preparation of whole tumor cell vaccine*

TBS (0.5 mg), DSPE-PEG2000 (2.5 mg), and DSPE-PEG2K-PEI800 (2.5 mg) were dissolved in 1 mL THF and mixed uniformity under ultrasound conditions used as the work solution. The above work solution was added dropwise slowly into 9 mL of purified water. After further overnight stirring in the fume hood, the resultant solution was purified with 0.22 μm filtration. Then, the resulting p-TBS NPs were stored in a 4 °C freezer for the following usage. The 4T1 tumor cells were incubated with p-TBS NPs at a concentration of 80 μg/mL. Changed the culture medium after 4 h, and irradiated with a 1064 nm laser (1 W/cm^2) for 15 min. The treated cells were collected and frozen at −20 °C for 2 h. It is put back in the 37 °C-cell incubator to restore the temperature and conduct the freeze-thaw cycle again. After two times, all cells were centrifuged at 2000 rpm for 5 min. Collected the precipitate and counted.

2.4. *Animals*

All the animal experiments were approved by the Animal Ethics Committee of Soochow University and City University of Hong Kong (Project No. CityU 11300320).

2.5. *4T1-tumor occurrence prevention*

Mice were randomly divided into five groups. Two subcutaneous injections (days 0 and 3) of PBS or NIR-II NV (1×10^6, 100 μL) were given respectively. Mice of the NIR-II NV + L group were irradiated by a 1064 nm laser (1 W/cm^2) for 15 min in the left lymph node. On the 4th day, the offside-tumor occurrence model was established by subcutaneously inoculating mouse breast cancer cells 4T1 (1×10^6) on the right side of the mouse. The lung metastasis-tumor occurrence model was established by injecting 4T1 (5×10^5) into the tail vein of mice.

3. Results

3.1. *NPs preparation and optical characterization*

TBS was synthesized by utilizing triphenylamine (TPA) as the donor (D) fragment, thiophene unit as the conjugation bridge (*π*), and strongly electron-withdrawing selenium-monosubstituted benzo[1,2-*c*:4,5-*c*′]bis ([1,2,5]thiadiazole) (Se-BBT) as acceptor (A) (Fig. 1). In each TBS molecule, the two TPA units provide many rotatable benzene rings, which serve as effective energy dissipators to the molecule upon excitation. The synthetic pathway is listed in Supporting Information Fig. S1, and the chemical construction of the final product was well characterized *via* NMR and high-resolution MS (Supporting Information Figs. S2−S4). The absorption spectrum in the UV−Vis−NIR region of TBS indicates that TBS has an absorption maximum at 1010 nm with a molar absorption coefficient (*ε*) of 3.1 × 10^4 M^{-1} cm^{-1} (Supporting Information Fig. S5). As demonstrated by density functional theory (DFT), the energies of the highest occupied molecular orbital (HOMO) and the lowest unoccupied molecular orbital (LUMO) of TBS were measured to be −4.68 and −3.42 eV, respectively, suggesting a low energy gap (1.26 eV). DFT calculations revealed that TBS has a large dihedral angle between triphenylamine and thiophene (Supporting Information Fig. S6). These results suggest that TBS has good light-harvesting properties over the NIR-II window and exhibits good potential for NIR-II theranostics.

To make TBS more versatile for theranostics applications, the amphiphilic copolymer DSPE-PEG$_{2000}$ was used to co-assemble the hydrophobic TBS molecules into water-dispersive nanoparticles (TBS NPs) *via* the standard nanoprecipitation technique (Fig. 2A). As expected, the TBS NPs exhibited broad optical absorption at 800−1200 nm, with an absorption maximum of 913 nm (Fig. 2B). Dynamic light scattering (DLS) measurements revealed that the TBS NPs had a hydrodynamic size of approximately 100 nm and uniform distribution with a polydispersity index (PDI) of 0.18 (Fig. 2C). Transmission electron microscopy (TEM) revealed that the TBS NPs had a spheroid morphology with a size of approximately 50 nm, which possibly ascribed to the absence of a hydration layer on the surface of the NPs. The sizes of the TBS NPs remained almost unchanged after 30 days of storage in water and PBS solution (Supporting Information Figs. S7 and S8), which would benefit from the negative surface charge of −50.3 mV (Supporting Information Fig. S9). Moreover, the TBS NPs in water showed good diradical properties that were similar to free TBS in THF, indicating their open-shell and radical features (Fig. 2D).

3.2. *Photothermal properties and theoretical calculations of nanoparticles*

Next, we further studied the photothermal conversion properties of the TBS NPs under the NIR-II excitation. The temperature increase of the TBS NP aqueous solution at different irradiation times is shown in Fig. 2E (red dots) and F. For comparison, we also included NPs made with an oligomer (FBS, blue dots) of a similar molecular structure (Supporting Information Fig. S10). Without any NPs, water (black dots) only caused mild temperature changes, indicating that the temperature increases in the two NP

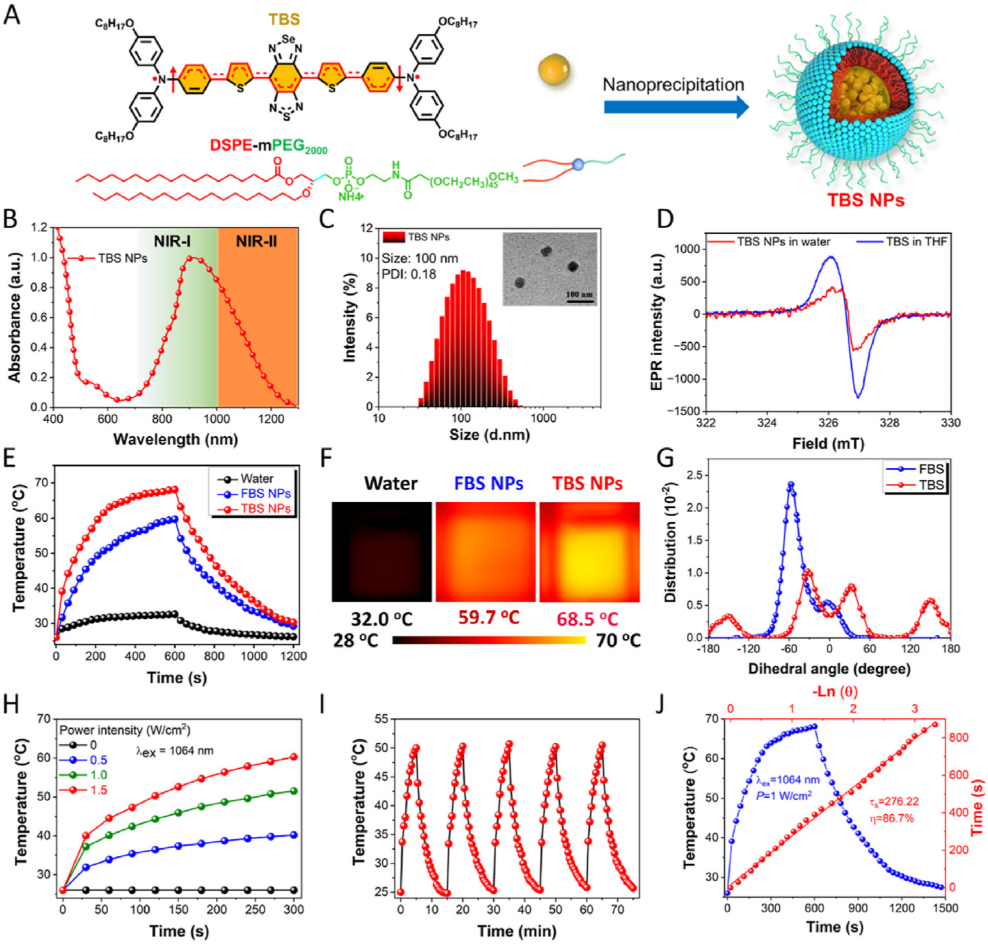

Figure 2 Photothermal properties and theoretical calculations of nanoparticles. (A) Diagrammatic drawing of the NP fabrication. (B) Absorption spectrum of the TBS NPs. (C) DLS data and TEM picture of TBS NPs. (D) Radical characteristics of TBS in THF and TBS NPs in water. (E) Temperatures of TBS NPs (100 μg/mL) and FBS NPs (100 μg/mL) aqueous dispersions under 1064 nm light illumination (1 W/cm^2) for 10 min. (F) Infrared thermal imaging of (E) various samples upon 10 min of illumination. (G) Calculated dihedral angle distributions in the aromatic rings of TBS (red) and FBS (blue). (H) Heating curves of TBS NPs (50 μg/mL) upon 1064 nm illumination of different power intensities. (I) Photothermal stability of TBS NPs (50 μg/mL) within five cycles of light illumination by 1064 nm laser (1 W/cm^2). (J) Temperature variation and PCE calculation of TBS NPs (100 μg/mL) aqueous dispersion after 10 min illumination of 1064 nm laser (1 W/cm^2).

dispersions were mainly caused by the NPs. The most important difference between TBS and FBS is that there are many more rotatable units in TBS. We then determined the distributions of the dihedral angles in TBS and FBS (Fig. 2G) using molecular dynamics simulations. The TBS has large dihedral angles with a wide distribution between −180 and 180 °C, while that of FBS is mainly located in a relatively narrow distribution in the range of −120 to 60 °C. This suggests that rotations of molecular moieties are generally easier in TBS. This was further confirmed by the instantaneous torsion evolution of TBS and FBS and the geometries of TBS optimized by molecular dynamics simulation in the aggregate state (Supporting Information Figs. S11 and S12). These experiments suggested that the introduction of molecular rotations can enhance molecular motion to boost photothermal conversion performance.

It is worth noting that the TBS NP aqueous solution reached a maximum temperature of 68.5 °C after 10 min irradiation of a 1064 nm laser (1 W/cm^2). Under the same conditions, the FBS NP dispersion only reached a temperature of 59.7 °C, verifying the superior photothermic property of the TBS NPs. Laser density-dependent and concentration-dependent temperature increases of TBS NPs were demonstrated under the same laser conditions (Fig. 2H and Supporting Information Fig. S13). Notably, after five cycles of 5 min irradiation of 1064 nm laser (1 W/cm^2) and free cooling to ambient temperature, the variations in the temperature increase of the TBS NPs were negligible (Fig. 2I). Furthermore, the absorption spectrum and solution color remained unchanged after five heating−cooling cycles, revealing the outstanding photostability of the TBS NPs (Supporting Information Figs. S14 and S15). Moreover, the negligible diameter changes of the TBS NPs after laser irradiation further confirmed their photothermal stability (Supporting Information Fig. S16). The PCE of TBS NPs was evaluated by measuring according to the reported procedure (Fig. 2J). The PCE of TBS NPs reached 87%, while the PCE of FBS NPs reached 70.1% (Supporting Information Fig. S17). To our knowledge, the PCE value of the TBS NP dispersion is the highest among all reported PTAs upon excitation with light beyond 1000 nm (Supporting Information Table S1). Considering the TBS NPs simultaneously possess NIR-I and NIR-II absorption, we evaluated the photothermal performance of TBS NPs excited by an 808 nm laser. Upon 808 nm laser irradiation, TBS NPs showed a relatively poor temperature rise and PCE, which was much lower than that for 1064 nm laser (Fig. S18−S20). The record-high NIR-II photothermal conversion effect of TBS NPs under 1064 nm laser benefits from their low energy loss *via* radiative transition and flexible intramolecular motion within π-conjugated oligomers for enhancing nonradiative transition.

3.3. *In vitro phototherapy performance*

Considering the good NIR-II photothermic effect, TBS NPs were applied to quantitatively investigate the *in vitro* photothermal elimination of tumor cells using a standard 3-(4,5-dimethylthiazol-2-yl)-2,5-diphenyltetrazolium bromide (MTT) assay. As shown in Fig. 3A and Supporting Information Fig. S21, human lung cancer (A549) cells incubated with various concentrations (0−50 μg/mL) of TBS NPs displayed negligible cell death even at a high concentration of 50 μg/mL, suggesting the nice biological compatibility of the TBS NPs. In contrast, upon 5 min illumination of a 1064 nm laser (1 W/cm^2), the A549 cells incubated with TBS NPs were availably eliminated *via* the photothermal ablation, with a concentration-dependent profile. As expected, impressive photothermal ablation performance was also confirmed in murine breast cancer cells (4T1), which achieved approximately >95% cancer cell elimination upon 1064 nm laser illumination (Fig. 3B and Supporting Information Fig. S22). However, 808 nm laser irradiation showed a weaker photothermal ablation effect on A549 cells than 1064 nm laser irradiation with the same TBS NPs concentration (Supporting Information Fig. S23). Then, live/dead cell staining was employed to visualize the photoablation effect of TBS NPs on cancer cells (Fig. 3C and Supporting Information Figs. S24 and S25). The Calcein AM (green fluorescence) and propidium iodide (PI, red fluorescence) represented live and dead cells, respectively under confocal imaging. Neither the laser alone nor the NPs alone induced any effect on cell viability. In comparison, upon 1064 nm irradiation, the photoablation effect on cell survival improved with increasing irradiation time, and almost all 4T1 cells were killed when the irradiation time reached 10 min. All the results indicate the advantageous photothermal ablation of *in vitro* cancer cell elimination by TBS NPs.

3.4. *In vitro photoacoustic performance*

In vitro and *in vivo* NIR-II photoacoustic imaging (PAI) capability under excitation by a 1064 nm pulsed laser was then examined. The photoacoustic amplification of TBS NPs at various concentrations from 0 to 200 μg/mL was performed with a photoacoustic computed tomography (PACT) system. As depicted in Fig. 4A and B, the TBS NPs showed strong photoacoustic signals with a good linear correlation to concentration, even below 6.25 μg/mL. We then filled a PA-free capillary with a TBS NP dispersion of 100 μg/mL to measure the PA intensity under different wavelength excitations (Fig. 4C). Among the multiwavelength excitations, the 1064 nm laser generates the strongest PA signal with the same excitation fluence, and the PA spectrum was profiled to indicate that the TBS NPs have broad PA-responsive performance in the NIR-II range, with a PA maximum of 1064 nm (Fig. 4D).

To further demonstrate the superiority of NIR-II PAI, we applied chicken breast muscles of various thicknesses to examine the deep-tissue penetration performance. As shown in Fig. 4E−G, TBS NPs under 1064 nm excitation exhibited considerably deeper penetration than those under 808 nm excitation, which suggested that TBS NPs are qualified candidates for NIR-II PAI probes. *In vivo* PAI was further performed on tumor-xenograft mice to image the tumor-targeting ability of TBS NPs after tail vein injection. As illustrated in Fig. 4H, the PA signal at 1064 nm tended to increase after intravenous administration of TBS NPs, and the peak value of the PA signal was realized at 12 h postinjection (approximately 5-fold enhancement). Notably, the PA signal at the tumor site had a sufficiently strong retention effect after 18 h of injection and showed greatly reduced signal strength at 24 h postinjection, suggesting good tumor-targeting performance (Fig. 4I).

3.5. *In vivo photothermic performance*

To evaluate the *in vivo* photothermic performance, intravenous injections of TBS NP dispersions (5 mg/kg) were administered to 4T1 tumor-xenograft model mice, which were then anesthetized for 5 min irradiation with a 1064 nm laser (1 W/cm^2). An infrared thermal image was employed to capture the temperature evolution of the tumor location at different irradiation times (Fig. 5A), and the detailed variations in temperature were also measured as a

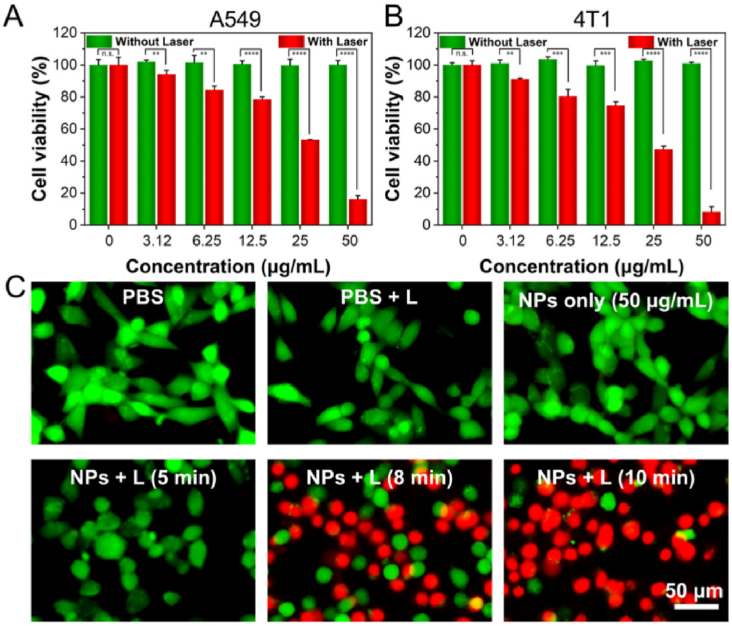

Figure 3 *In vitro* phototherapy performance. (A) *In vitro* cell killing of A549 and (B) 4T1 cells after incubation with TBS NPs with or without 1064 nm laser irradiation at 1.0 W/cm^2 for 5 min. (C) Fluorescence imaging of live/dead 4T1 cells under various treatment conditions. The green and red fluorescence respectively represent live cells and dead cells. Data are presented as mean ± SD ($n = 3$, $^{**}P < 0.01$, $^{***}P < 0.001$, $^{****}P < 0.0001$). n.s.: not significant.

function of irradiation time (Fig. 5B). The tumor-site temperatures of TBS NPs-treated mice quickly increased from 30 to 65 °C within 5 min irradiation of a 1064 nm laser. In contrast, when PBS was injected instead of the NPs, the tumor-site temperatures increased by only ∼5 °C under the same illumination. We subsequently launched *in vivo* therapeutic experiments to evaluate the *in vivo* photothermal ablation of tumors. When 4T1 tumor-xenografted mice reached a size of approximately 100 mm^3, the mice were randomized into four groups: PBS, PBS + laser (PBS + L), NPs, and NPs + laser (NPs + L) groups. 1 W/cm^2 of 1064 nm laser irradiation was performed for 5 min at 12 h post-injection of TBS NPs. The tumor sizes of the four groups were continuously recorded every 2 days by an electronic digital caliper, and photographs of the tumors from the treated mice were acquired after 14 days (Fig. 5C). Mice in the PBS + L and NPs groups showed nearly identical tumor growth trends as those in the PBS group. However, tumors in the NPs + L group had almost complete tumor elimination after treatment (Fig. 5D), revealing the superior photothermic therapeutic performance of the TBS NPs. Tumor weight analysis after 14 days of treatment further confirmed that the photothermic effect of TBS NPs effectively eliminated the tumor traces (Fig. 5E). Moreover, low-temperature PTT ablation of TBS NPs was also conducted and found that the treated tumors achieved effective ablation with obvious recurrent (Supporting Information Fig. S26). We then investigated the photothermic effect on tumor tissue with hematoxylin and eosin (H&E) staining and terminal deoxynucleotidyl transferase d-UTP nick end labeling (TUNEL) assay. As shown in Fig. 5F, photothermic treatment with TBS NPs triggered apparent apoptosis in the tumors but not in the other groups, including the PBS + L and NP-only groups, in which tumor cells of tumor location were almost completely ablated. These *in vivo* therapeutic trials demonstrated that TBS NPs activated with the NIR-II laser can efficiently eliminate tumors.

3.6. *In vivo biocompatibility*

Furthermore, the *in vivo* toxicology of the TBS NPs was systematically investigated. After TBS NPs + laser treatment, the mice maintained normal behaviors with no adverse events. Moreover, all treated mice exhibited negligible variations in body weight within the treatment, suggesting that these treatments had insignificant adverse effects (Supporting Information Fig. S27). The major organs, such as the heart, liver, spleen, lung, and kidney, were subjected to tissue biopsy with standard H&E staining, and no obvious alterations in histological parameters were observed in the treated mice (Fig. 5F), which suggested that TBS NPs administration and NIR-II laser irradiation did not induce any noticeable negative effects. Photos of treated mice after 14 days also proved the skin (Supporting Information Fig. S28). Additionally, hematological marker and biochemical index analyses of relatively good biocompatibility of the TBS NPs + laser treatment toward surroundings were also performed and confirmed that the TBS NPs-treated group showed similar microstructure characteristics with the PBS-treated group (Supporting Information Fig. S29), further confirming the good biocompatibility of the TBS NPs.

3.7. *In vivo tumor treatment of NIR-II-activated vaccine*

Early prevention of tumor occurrence is another major challenge in the field of tumor treatment and prevention. Tumor vaccines can induce tumor-specific immune stimulation and thus achieve efficient tumor prevention, which has been deemed a promising strategy for immunotherapy-based cancer prevention. Next, we utilized the resulting NIR-II responsive TBS NPs to design a NIR-II activated whole-cell vaccine (NIR-II NV). For NIR-II NV preparation, polyethyleneimine (PEI)-modified TBS NPs (p-TBS NPs) with good biocompatibility were successfully prepared (Supporting Information Figs. S30−S33).

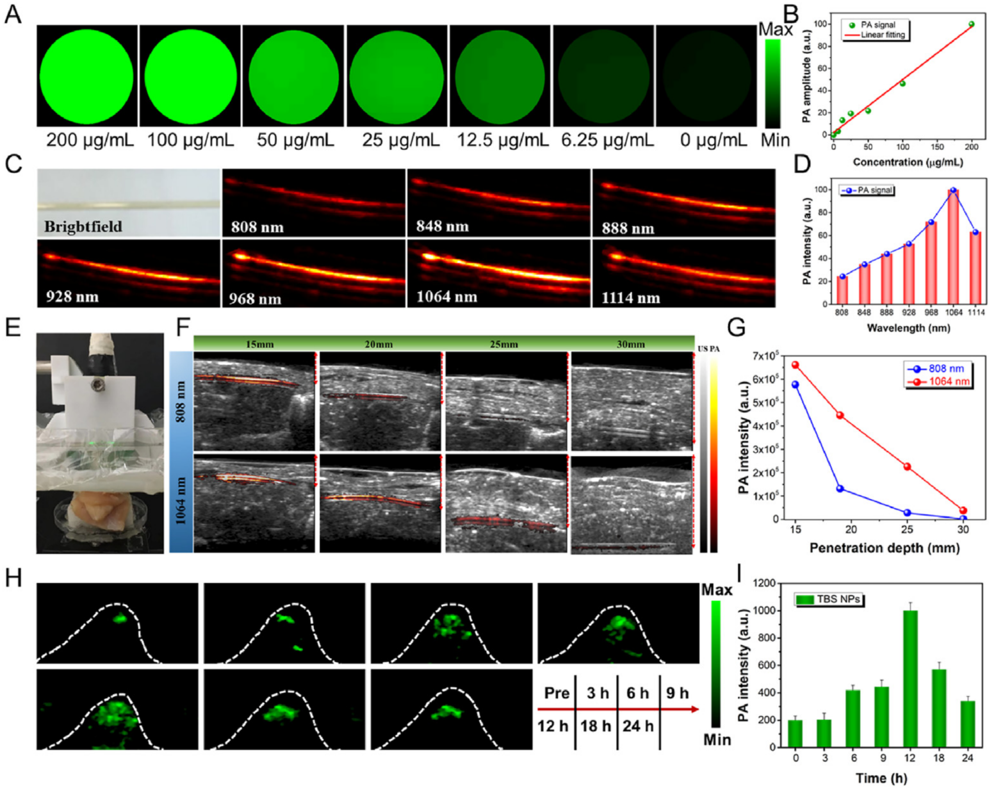

Figure 4 *In vitro* photoacoustic performance. (A) *In vitro* PA phantoms and (B) relative PA signal amplification as a function of TBS NPs concentrations (R^2 = 0.996, wavelength = 1064 nm). (C) PA imaging and (D) relative PA spectra at different wavelengths of the TBS NPs aqueous dispersion filled in a capillary tube. (E) PACT installation and (F) PA imaging of TBS NPs after being covered by various thicknesses of chicken. PA images were captured under the excitation of NIR-I (808 nm) and NIR-II (1064 nm) laser of the same power (10.0 mJ/cm^2). (G) Corresponding PA intensity of chickens of various thicknesses. (H) *In vivo* PA imaging and (I) relative intensities of PA signals towards tumor at different times after TBS NPs postinjection.

Compared with TBS NPs, p-TBS NPs showed enhanced uptake in 4T1 cells under the same conditions (Supporting Information Figs. S34 and S35). As shown in Fig. 6A, to prepare the NIR-II NV, TBS NPs with a positive charge were loaded into tumor cells, and NIR-II light was applied to induce the tumor cells with endogenous adjuvants. Then, a freeze-thaw operation was applied to inactivate the resulting NIR-II NV to yield a safe vaccine. Cell imaging demonstrated that the NIR-II NV subjected to freeze-thaw treatment exhibited complete cell death and simultaneously contained efficient p-TBS NPs in the cytoplasm (Fig. 6A and Supporting Information Fig. S36). Upon irradiation with 1064 nm light, the temperature of the NIR-II NV mildly increased in a cell population-dependent manner (Fig. 6B and Supporting Information Fig. S37). To further explore the formation of NIR-II NV, we identified differentially expressed genes (DEGs) by performing RNA sequencing of 4T1 cells with or without p-TBS NPs treatment and 1064 nm light irradiation and analyzed the DEGs by Gene Ontology (GO) enrichment analysis and Kyoto Encyclopedia of Genes and Genomes (KEGG) enrichment protocols. As illustrated in Fig. 6C and D, compared PBS group, only laser (LT group), and p-TBS NPs (T-N group) groups, the cells in the NIR-II NV group contained 709 DEGs, of which 428 DEGs were upregulated and 281 DEGs were efficiently downregulated. Notably, the NIR-II NV upregulated the expression of *Mmp1b*, *Cd79a*, *Cd109*, *Hspa4l*, *Il11*, *Atf4*, *Tnfsf18*, and other immune activation-related genes. KEGG enrichment analysis further demonstrated that the DEGs in the NIR-II NV were enriched in apoptosis-related pathways (such as the *p53* signaling pathway) and immune response-related pathways (such as tumor necrosis factor (*TNF*) signaling pathway, cytokine−cytokine receptor interaction pathway, nuclear factor-κB (NF-κB) signaling pathway, and *IL17* signaling pathway) (Supporting Information Fig. S38). These experiments suggest that the NIR-II NV with 1064 nm light irradiation could efficiently induce cell apoptosis and immunogenic protein release, confirming the effectiveness of the light-activated whole-cell vaccine.

Next, the NIR-II NV vaccine was applied to prevent cell occurrence *via* subcutaneous (s.c.) injection of the vaccine and 1064 nm light irradiation, after which 4T1 tumors were inoculated at the distal end (Fig. 6E). After twice s.c. injections of NIR-II NV and twice 1064 nm light irradiation, the percentages of CD4$^+$ and CD8$^+$ T cells in the inguinal lymph nodes of the NIR-II NV and NIR-II NV plus light irradiation (NIR-II NV + L) treatment groups were greater than those in the PBS and cell vaccine without NIR-II light irradiation (NV) groups, indicating efficient immune activation (Fig. 6F, Supporting Information Figs. S39 and S40). There was an obvious increase in the *IFN-γ*, *TNF-α*, and *IL-6* levels in the serum of the NIR-II NV and NIR-II NV + L treated mice compared with those in the PBS and NV-treated mice (Fig. 6G−I). Notably, compared with the NIR-II NV alone, the NIR-II NV with 1064 nm light irradiation exhibited more effective immune activation, demonstrating that the combination of the NIR-II NV and 1064 nm light irradiation could enhance the efficacy of the vaccine *via* local and mild photothermal conversion.

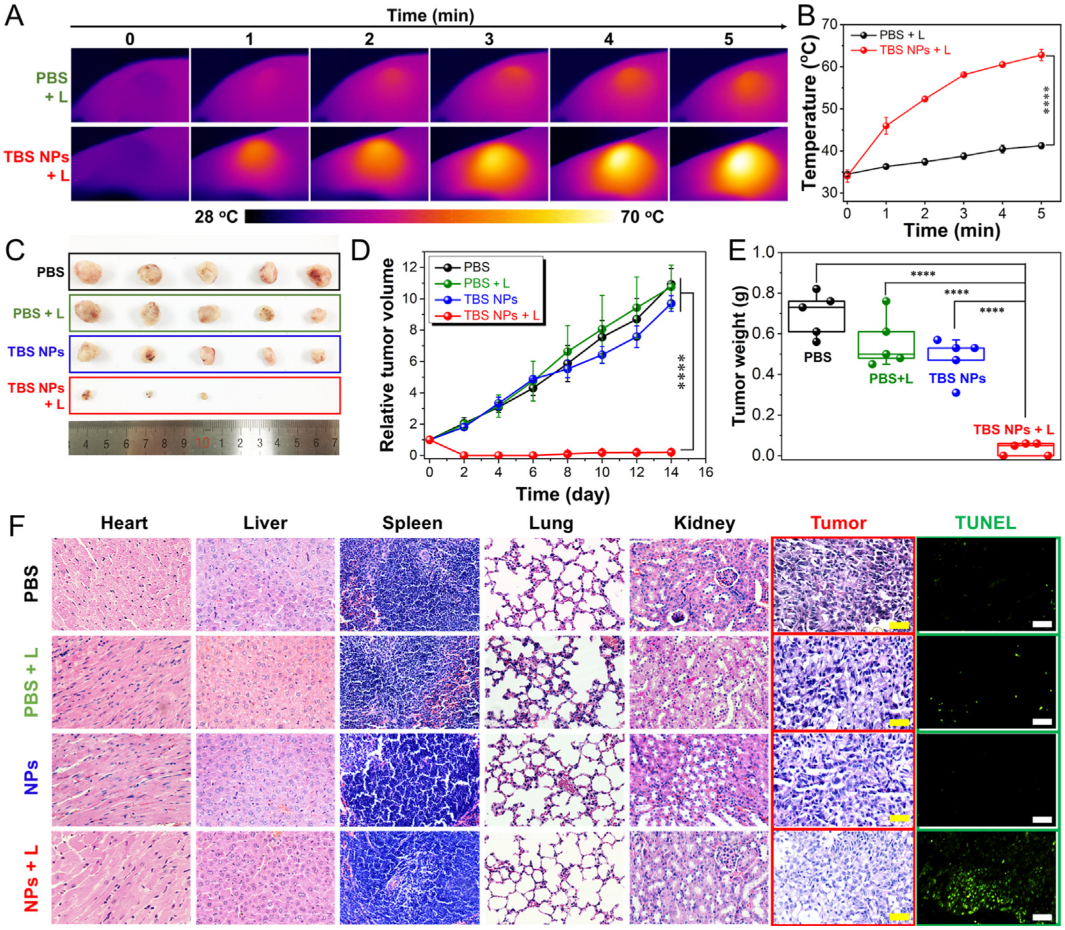

Figure 5 *In vivo* photothermic performance. (A) Representative thermal photographs and (B) relative temperature profiles of tumors from the mice with various treatments. (C) Tumor images of the treated mice after 14-day treatments. (D) The relative volume of tumors from different treatment groups within 14-day treatments. (E) Weight changes in tumors. (F) H&E and TUNEL staining of the major organs and tumors from the mice with various treatments. Scale bar = 50 μm. Data are presented as mean ± SD ($n = 5$, ****$P < 0.0001$).

After NIR-II NV vaccination, the growth of distal 4T1 tumors was further monitored, and the data found that the growth of tumors in the mice in the NIR-II NV and NIR-II NV + L groups was suppressed compared with that in the PBS and NV groups (Fig. 6J and Supporting Information Figs. S41−S43). Notably, tumor inhibition analysis revealed that the NIR-II NV + L had more effective tumor prevention effects than NIR-II NV without 1064 nm light irradiation, which might be attributed to the mild increase in antigen release and immune activation induced by 1064 nm light irradiation (Supporting Information Fig. S44). The infiltration of $CD8^+$ T cells (cytotoxic T cells) and $CD45RA^+$ T cells (memory T cells) in the tumor site was further tested by immunofluorescence on the 20th day after treatment (Fig. 6K). The results showed that the tumors of the NIR-II NV + L treated mice exhibited the most effective infiltration of $CD8^+$ T cells and $CD45RA^+$ T cells among the four groups, which further confirmed the effective immune activation induced by vaccination. In addition, the good biological safety of the NIR-II NV was further confirmed by the almost unchanged weight of the treated mice during the full course of treatment (Supporting Information Fig. S45). The results demonstrated that NIR-II NVs preactivated with 1064 nm light could provide an efficient vaccination for cancer prevention, and this vaccination effect could be further improved by 1064 nm light irradiation at the tumor nidus. Thus, these results indicate the enhanced efficiency of the NIR-II light-activated whole-cell vaccine.

3.8. *In vivo tumor prevention of NIR-II activated-vaccine*

Taking advantage of the remarkable tumor prevention potential of the NIR-II NV, the tumor metastasis prevention potential of the NIR-II NV was further investigated and shown in the treatment schedule in Fig. 7A. After two vaccinations and local 1064 nm light irradiation, lung metastasis was established by intravenous injection of 4T1 cells, and the treatment efficiency was continuously monitored.

As listed in Fig. 7B and Supporting Information Fig. S46, the number of $CD8^+$ T cells in the lymph nodes of the mice was effectively increased by the NIR-II NV and NIR-II NV + L vaccination. Additionally, the serum levels of proinflammatory cytokines (IL-6, TNF-α, and IFN-γ) increased significantly after two rounds of vaccination with the NIR-II NV and NIR-II NV + L, which further indicated that NIR-II NV and NIR-II NV + L efficiently induced strong immunostimulatory effects (Fig. 7D−F). Lung tissues were extracted from the mice to evaluate lung tumor metastasis at 20 days posttreatment, and the

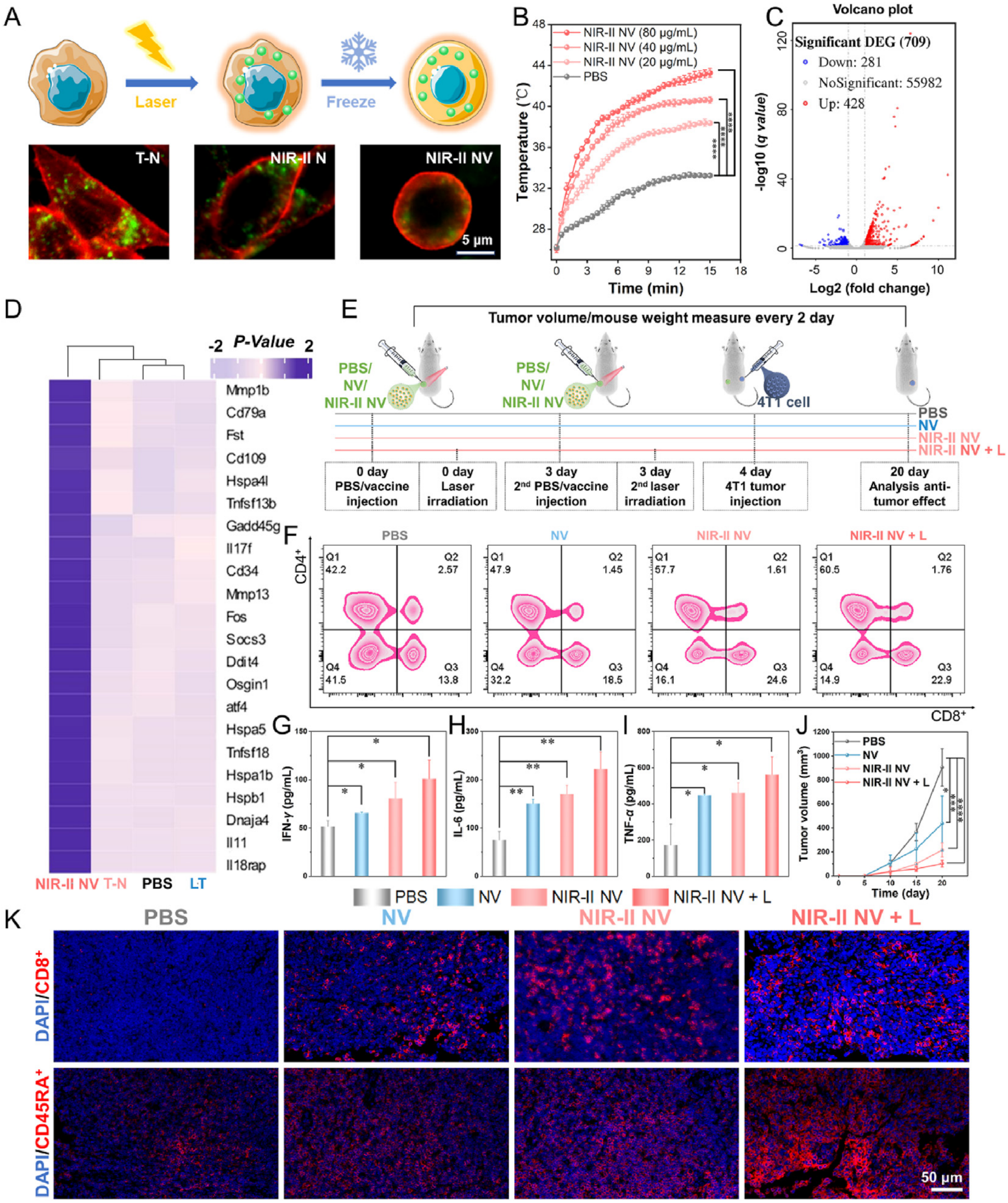

Figure 6 *In vivo* tumor treatment of NIR-II activated vaccine. (A) Vaccine preparation and cell imaging of the NIR-II NV construct. (B) Temperature changes of the NIR-II NVs (10^7 cells/mL, 500 μL) after incubation with different concentrations of TBS NPs exposed to 15 min laser irradiation of 1064 nm (1 W/cm^2). (C) Volcano plot of all DEGs in the NIR-II NV-treated cells. (D) Heatmap of differential gene cluster analysis of the treated cells. (E) Schematic diagram of tumor prevention by the NIR-II NV-based vaccine. (F) Analysis of CD4$^+$ T and CD8$^+$ T cells in the lymph nodes of mice on the 4th day after treatment. (G–I) Analysis of G) IFN-γ, H) IL-6, and I) TNF-α in mouse serum on the 4th day after treatment. (J) Tumor volume changes of the treated mice within the treatment. (K) Infiltration levels of CD8$^+$ T cells (cytotoxic T cells) and CD45RA$^+$ T cells (memory T cells) in the tumor sites on the 20th day posttreatment. Data are presented as mean ± SD (n = 3 in B and G–I, n = 4 in J, *$P < 0.05$, **$P < 0.01$, ***$P < 0.001$, ****$P < 0.0001$).

results found that compared with PBS, the NIR-II NV and NIR-II NV + L vaccines significantly inhibited the proliferation and metastasis of breast cancer cells in the lung. NIR-II NV + L achieved 80% inhibition of pulmonary nodules, which was slightly greater than that achieved with the NIR-II NV alone (Fig. 7C and G). H&E biopsy of the lung further confirmed the efficient prevention and suppression of tumor metastasis by the NIR-II-activated vaccine (Fig. 7H). Moreover, H&E staining of the main organs, blood biochemical index analysis, and body weight changes of the mice subjected to various treatments demonstrated the good *in vivo* biosafety of the NIR-II-activated vaccine (Supporting Information Figs. S47–S49). These results demonstrated the high-performance efficiency and biosafety of the NIR-II-activated vaccine in preventing tumor metastasis.

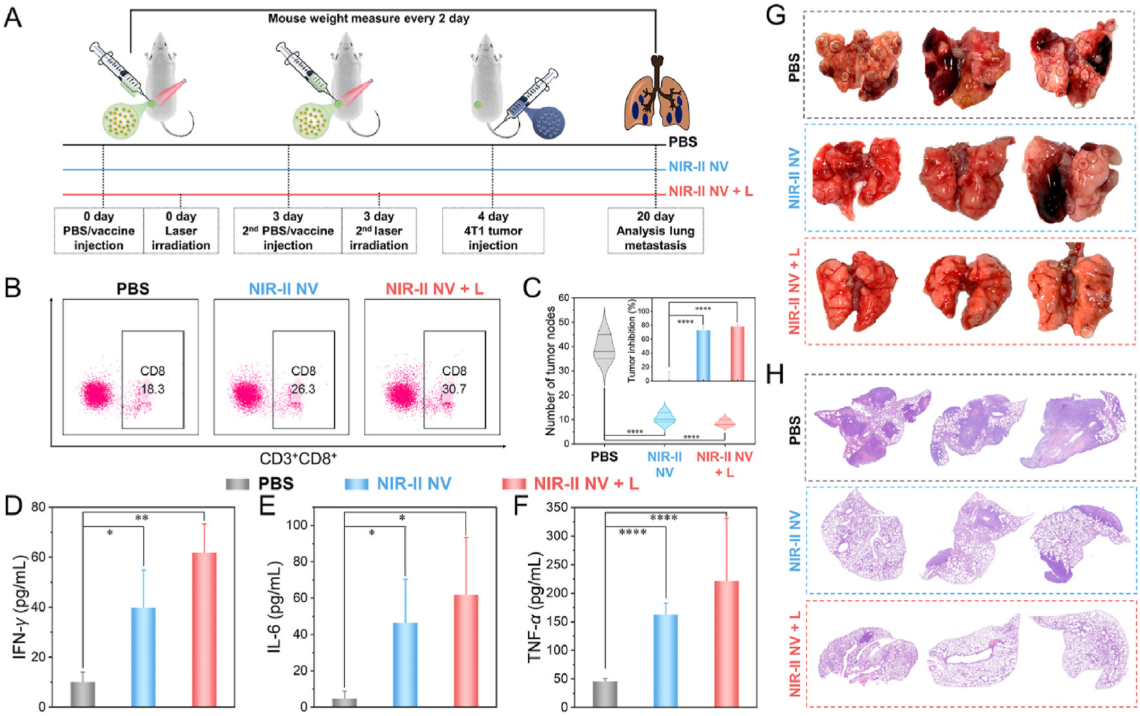

Figure 7 *In vivo* tumor prevention of NIR-II activated vaccine. (A) Schematic diagram of lung metastasis-tumor inhibition by the NIR-II NV-based vaccine. (B) Quantitative test of CD8$^+$ T cells in the lymph nodes of the treated mice on the 4th day after treatment. (C) Number statistics of tumor nodes in the lung and the tumor inhibition rate in the mice on the 20th day after treatment. (D−F) Analysis of (D) IFN-γ, (E) IL-6, and (F) TNF-α in mouse serum on the 4th day after treatment. (G) Representative photographs of the lung from the treated mice. (H) H&E photographs of the lung in the different groups. Data are presented as mean ± SD ($n = 3$, $^*P < 0.05$, $^{**}P < 0.01$, $^{****}P < 0.0001$).

4. Conclusions

We developed an efficient NIR-II nanoplatform by introducing flexible motors into semiconducting biradical oligomers for high-performance cancer photo theranostics and vaccination *in vivo*. The semiconducting biradical oligomer TBS offers maximum absorption of over 1000 nm and flexible molecular motors and thus provides a record-breaking PCE of 87% upon NIR-II light illumination at 1064 nm. Taking advantage of the inherent NIR-II performance of TBS, we also showed that the biocompatible TBS-based nano platform achieved highly efficient PAI and PTT of tumors in the NIR-II window. With these advantages, the TBS nano platform was further applied to produce a simple NIR-II-activated whole-cell vaccine. NIR-II-activated whole-cell vaccines can effectively enhance the antitumor immune response *in vivo* and are highly effective at preventing cancer and inhibiting metastasis in breast carcinoma with high biosafety. This semiconducting biradical oligomer nano platform may work as a universal proof to explore new NIR-II nano vaccines with NIR-II-controlled capability and open up new avenues for personalized cancer vaccines.

Acknowledgments

This work was financially supported by the National Natural Science Foundation of China (No. 52173135), the Natural Science Foundation of Jiangsu Province (No. BK20231523, China), Jiangsu Specially Appointed Professorship, Leading Talents of Innovation and Entrepreneurship of Gusu (ZXL2022496, China), and the Suzhou Science and Technology Program (SKY2022039, China). Chun-Sing Lee thanks the support of the Research Grants Council of Hong Kong Special Administrative Region, General Research Fund (No. CityU 11300320, 11318322, China). Prof. Lidai Wang acknowledges support from the National Natural Science Foundation of China (No. 81627805) and the Research Grants Council of the Hong Kong Special Administrative Region (21205016, 11215817, 11101618, China). The authors would also like to acknowledge the project funded by the Priority Academic Program Development (PAPD) of Jiangsu Higher Education Institutions and Suzhou International Joint Laboratory for Diagnosis and Treatment of Brain Diseases.

Author contributions

Yijian Gao: Writing − review & editing, Writing − original draft, Visualization, Methodology. Yachao Zhang: Writing − review & editing, Visualization, Methodology. Yujie Ma: Writing − review & editing, Visualization, Methodology. Xiliang Li: Writing − review & editing, Methodology, Writing − review & editing, Methodology. Yu Wang: Writing − review & editing, Methodology. Huan Chen: Writing − review & editing, Methodology. Yingpeng Wan: Writing − review & editing, Methodology. Zhongming Huang: Writing − review & editing, Methodology. Weimin Liu: Writing − review & editing, Methodology. Pengfei Wang: Writing − review & editing, Methodology. Lidai Wang: Writing − review & editing, Supervision, Project administration, Methodology. Chun-Sing Lee: Writing − review & editing, Supervision, Project administration. Shengliang Li: Writing − review & editing, Writing − original draft, Supervision, Project administration, Methodology.

Conflicts of interest

The authors have no conflicts of interest to declare.

Appendix A. Supporting information

Supporting information to this article can be found online at https://doi.org/10.1016/j.apsb.2024.12.017.

References

1. Liang JL, Jin XK, Luo GF, Zhang SM, Huang QX, Lin YT, et al. Immunostimulant hydrogel-guided tumor microenvironment reprogramming to efficiently potentiate macrophage-mediated cellular phagocytosis for systemic cancer immunotherapy. *ACS Nano* 2023;**17**:17217−32.
2. Zu MH, Ma Y, Zhang J, Sun JF, Shahbazi MA, Pan GQ, et al. An oral nanomedicine elicits α vaccination effect against colorectal cancer. *ACS Nano* 2024;**18**:3651−68.
3. Ye JJ, Bao P, Deng K, Dong X, He JL, Xia Y, et al. Engineering cancer cell membranes with endogenously upregulated HSP70 as a reinforced antigenic repertoire for the construction of material-free prophylactic cancer vaccines. *Acta Biomater* 2024;**174**:386−99.
4. Liu XQ, Huang P, Yang RS, Deng HZ. mRNA cancer vaccines: construction and boosting strategies. *ACS Nano* 2023;**17**:19550−80.
5. Chen M, Li HJ, Zang J, Deng YY, Li HJ, Wu Q, et al. Potentiating cancer vaccination by adjuvant-loaded cryo-shocked tumor cells. *Biomaterials* 2023;**302**:122319.
6. Kantoff PW, Higano CS, Shore ND, Berger ER, Small EJ, Penson DF, et al. Sipuleucel-T immunotherapy for castration-resistant prostate cancer. *N Engl J Med* 2010;**365**:411−21.
7. Bo Y, Wang H. Biomaterial-based *in situ* cancer vaccines. *Adv Mater* 2024;**36**:2210452.
8. Lin MJ, Svensson-Arvelund J, Lubitz GS, Marabelle A, Melero I, Brown BD, et al. Cancer vaccines: the next immunotherapy frontier. *Nat Cancer* 2022;**3**:911−26.
9. Anguille S, Smits EL, Lion E, Tendeloo VF, Berneman ZN. Clinical use of dendritic cells for cancer therapy. *Lancet Oncol* 2014;**15**:257−67.
10. Pérez-Baños A, Gleisner MA, Flores I, Pereda C, Navarrete M, Araya JP, et al. Whole tumour cell-based vaccines: tuning the instruments to orchestrate an optimal antitumour immune response. *Br J Cancer* 2023;**129**:572−85.
11. Sellars MC, Wu CJ, Fritsch EF. Cancer vaccines: building a bridge over troubled waters. *Cell* 2022;**185**:2770−88.
12. Meng JQ, Lv YL, Bao WE, Meng ZH, Wang S, Wu YB, et al. Generation of whole tumor cell vaccine for on-demand manipulation of immune responses against cancer under near-infrared laser irradiation. *Nat Commun* 2023;**14**:4505.
13. Guo B, Sheng ZH, Hu DH, Liu CB, Zheng HR, Liu B. Through scalp and skull NIR-II photothermal therapy of deep orthotopic brain tumors with precise photoacoustic imaging guidance. *Adv Mater* 2018;**30**: e1802591.
14. Chen BJ, Zhang CY, Wang WN, Chu ZY, Zha ZB, He XY, et al. Ultrastable $AgBiS_2$ hollow nanospheres with cancer cell-specific cytotoxicity for multimodal tumor therapy. *ACS Nano* 2020;**14**: 14919−28.
15. Shen S, Feng L, Qi SY, Cao J, Ge YR, Wu L, et al. Reversible thermochromic nanoparticles composed of a eutectic mixture for temperature-controlled photothermal therapy. *Nano Lett* 2020;**20**:2137−43.
16. Sun PF, Jiang XY, Sun B, Wang H, Li JW, Fan QL, et al. Electron-acceptor density adjustments for preparation conjugated polymers with NIR-II absorption and brighter NIR-II fluorescence and 1064 nm active photothermal/gas therapy. *Biomaterials* 2022;**280**:121319.
17. Xu GY, Bao X, Chen JQ, Zhang BH, Li D, Zhou D, et al. *In vivo* tumor photoacoustic imaging and photothermal therapy based on supra-(carbon nanodots). *Adv Healthc Mater* 2019;**8**:e1800995.
18. Yang C, Younis MR, Zhang J, Qu JL, Lin J, Huang P. Programmable NIR-II photothermal-enhanced starvation-primed chemodynamic therapy using glucose oxidase-functionalized ancient pigment nanosheets. *Small* 2020;**16**:e2001518.
19. Fan XX, Li YR, Feng Z, Chen GQ, Zhou J, He MB, et al. Nanoprobes-assisted multichannel NIR-II fluorescence imaging-guided resection and photothermal ablation of lymph nodes. *Adv Sci (Weinh)* 2021;**8**: 2003972.
20. Zhang H, Chen XX, Li SL, Shen JL, Mao ZW. An enhanced photothermal therapeutic iridium hybrid platform reversing the tumor hypoxic microenvironment. *Molecules* 2022;**27**:2629.
21. Zheng RJ, Zhao Q, Qing WX, Li SL, Liu ZH, Li QQ, et al. Carrier-free delivery of ultrasmall π-conjugated oligomer nanoparticles with photothermal conversion over 80% for cancer theranostics. *Small* 2022;**18**:e2104521.
22. Zhao YY, Song M, Yang XG, Yang J, Du CY, Wang GN, et al. Amorphous $Ag_{2-x}Cu_xS$ quantum dots: "all-in-one" theranostic nanomedicines for near-infrared fluorescence/photoacoustics dual-modal-imaging-guided photothermal therapy. *Chem Eng J* 2020;**399**:125777.
23. Lang F, Schrörs B, Löwer M, Türeci Ö, Sahin U. Identification of neoantigens for individualized therapeutic cancer vaccines. *Nat Rev Drug Discov* 2022;**21**:261−82.
24. Blass E, Ott PA. Advances in the development of personalized neoantigen-based therapeutic cancer vaccines. *Nat Rev Clin Oncol* 2021;**18**:215−29.
25. Cheng PF, Döll J, Romanus H, Wang HG, van Aken PA, Wang D, et al. Reactive magnetron sputtering of large-scale 3D aluminum-based plasmonic nanostructure for both light-induced thermal imaging and photo-thermoelectric conversion. *Adv Opt Mater* 2023;**11**: 2202664.
26. Shan BB, Lu YX, Zheng C, Li M. Structural symmetry effects in plasmonic metal-semiconductor hybrid heterostructures for multimodal cancer phototheranostics. *Chem Eng J* 2022;**444**:136707.
27. Younis MR, Wang C, An RB, Wang SJ, Younis MA, Li ZQ, et al. Low power single laser activated synergistic cancer phototherapy using photosensitizer functionalized dual plasmonic photothermal nanoagents. *ACS Nano* 2019;**13**:2544−57.
28. An D, Fu JY, Zhang B, Xie N, Nie GH, Ågren H, et al. NIR-II responsive inorganic 2D nanomaterials for cancer photothermal therapy: recent advances and future challenges. *Adv Funct Mater* 2021;**31**: 2101625.
29. Liu S, Pan XT, Liu HY. Two-dimensional nanomaterials for photothermal therapy. *Angew Chem Int Ed* 2020;**132**:5943−53.
30. Ouyang J, Feng C, Ji XY, Li L, Gutti HK, Kim NY, et al. 2D monoelemental germanene quantum dots: synthesis as robust photothermal agents for photonic cancer nanomedicine. *Angew Chem Int Ed* 2019; **131**:13539−44.
31. Shao JD, Zhang J, Jiang C, Lin J, Huang P. Biodegradable titanium nitride MXene quantum dots for cancer phototheranostics in NIR-I/II biowindows. *Chem Eng J* 2020;**400**:126009.
32. Wang XW, Wang XY, Yue QF, Xu HZ, Zhong XY, Sun LN, et al. Liquid exfoliation of TiN nanodots as novel sonosensitizers for photothermal-enhanced sonodynamic therapy against cancer. *Nano Today* 2021;**39**:101170.
33. Li L, Han X, Wang MF, Li CL, Jia T, Zhao XH. Recent advances in the development of near-infrared organic photothermal agents. *Chem Eng J* 2021;**417**:128844.
34. Li MH, Teh C, Ang CY, Tan SY, Luo Z, Qu QY, et al. Near-infrared light-absorptive stealth liposomes for localized photothermal ablation of tumors combined with chemotherapy. *Adv Funct Mater* 2015;**25**:5602−10.
35. Su MH, Han QJ, Yan XS, Liu YN, Luo P, Zhai WH, et al. Supramolecular strategy to engineering a non-photobleaching and near-Infrared absorbing nano-*J*-aggregate for efficient photothermal therapy. *ACS Nano* 2021;**15**:5032−42.
36. Zou Y, Liu WJ, Sun W, Du JJ, Fan JL, Peng XJ. Highly inoxidizable heptamethine cyanine−glucose oxidase conjugate nanoagent for combination of enhanced photothermal therapy and tumor starvation. *Adv Funct Mater* 2022;**32**:2111853.

37. Zhou HL, Tang DS, Kang XX, Yuan HT, Yu YJ, Xiong XL, et al. Degradable pseudo conjugated polymer nanoparticles with NIR-II photothermal effect and cationic quaternary phosphonium structural bacteriostasis for anti-infection therapy. *Adv Sci (Weinh)* 2022;**9**: 2200732.
38. Wu JYZ, Zhang YF, Jiang KJ, Wang XY, Blum NT, Zhang J, et al. Enzyme-engineered conjugated polymer nanoplatform for activatable companion diagnostics and multistage augmented synergistic therapy. *Adv Mater* 2022;**34**:e2200062.
39. Lyu Y, Zeng JF, Jiang YY, Zhen X, Wang T, Qiu SS, et al. Enhancing both biodegradability and efficacy of semiconducting polymer nanoparticles for photoacoustic imaging and photothermal therapy. *ACS Nano* 2018;**12**:1801−10.
40. Li M, Li Z, Yu DN, Wang M, Wang D, Wang B. Quinoid conjugated polymer nanoparticles with NIR-II absorption peak toward efficient photothermal therapy. *Chem Eur J* 2023;**29**:e202202930.
41. Chen M, Zhang XY, Liu JK, Liu F, Zhang RY, Wei PF, et al. Evoking photothermy by capturing intramolecular bond stretching vibration-induced dark-state energy. *ACS Nano* 2020;**14**:4265−75.
42. Duan XC, Zhang QY, Jiang Y, Wu XY, Yue X, Geng YH, et al. Semiconducting polymer nanoparticles with intramolecular motion-induced photothermy for tumor phototheranostics and tooth root canal therapy. *Adv Mater* 2022;**34**:e2200179.
43. Liu SJ, Zhou X, Zhang HK, Ou HL, Lam JWY, Liu Y, et al. Molecular motion in aggregates: manipulating TICT for boosting photothermal theranostics. *J Am Chem Soc* 2019;**141**:5359−68.
44. Zhu W, Kang MM, Wu Q, Zhang ZJ, Wu Y, Li CB, et al. Zwitterionic AIEgens: rational molecular design for NIR-II fluorescence imaging-guided synergistic phototherapy. *Adv Funct Mater* 2021;**31**:2007026.
45. Yan DY, Wang M, Wu Q, Niu N, Li M, Song RX, et al. Multimodal imaging-guided photothermal immunotherapy based on a versatile NIR-II aggregation-induced emission luminogen. *Angew Chem Int Ed* 2022;**61**:e202202614.
46. Zhao H, Huang YM, Lv FT, Liu LB, Gu Q, Wang S. Biomimetic 4D-printed breathing hydrogel actuators by nanothylakoid and thermoresponsive polymer networks. *Adv Funct Mater* 2021;**31**:2105544.
47. Yang N, Kang YT, Cong YJ, Wang XY, Yao C, Wang S, et al. Controllable gold nanocluster-emulsion interface for direct cell penetration and photothermal killing. *Adv Mater* 2023;**35**:e2208349.
48. He SS, Jiang YY, Li JC, Pu KY. Semiconducting polycomplex nanoparticles for photothermal ferrotherapy of cancer. *Angew Chem Int Ed* 2020;**59**:10633−8.
49. Wei X, Zhang C, He SS, Huang JG, Huang JS, Liew SS, et al. A dual-locked activatable phototheranostic probe for biomarker-regulated photodynamic and photothermal cancer therapy. *Angew Chem Int Ed* 2022;**61**:e202202966.
50. Zhou H, Zeng XD, Li AG, Zhou WY, Tang L, Hu WB, et al. Upconversion NIR-II fluorophores for mitochondria-targeted cancer imaging and photothermal therapy. *Nat Commun* 2020;**11**:6183.
51. Li YY, Zhang JQ, Liu SJ, Zhang C, Chuah C, Tang YH, et al. Enlarging the reservoir: high absorption coefficient dyes enable synergetic near infrared-II fluorescence imaging and near infrared-I photothermal therapy. *Adv Funct Mater* 2021;**31**:2102213.
52. Jiang ZY, Zhang CL, Wang XQ, Yan M, Ling ZX, Chen YC, et al. A borondifluoride-complex-based photothermal agent with an 80% photothermal conversion efficiency for photothermal therapy in the NIR-II window. *Angew Chem Int Ed* 2021;**60**:22376−84.
53. Wang XQ, Jiang ZY, Liang ZL, Wang TZ, Chen YC, Liu ZP. Discovery of BODIPY J-aggregates with absorption maxima beyond 1200 nm for biophotonics. *Sci Adv* 2022;**8**:5660.
54. Li JC, Yu XR, Jiang YY, He SS, Zhang Y, Luo Y, et al. Second near-infrared photothermal semiconducting polymer nanoadjuvant for enhanced cancer immunotherapy. *Adv Mater* 2021;**33**:e2003458.
55. Xu C, Pu KY. Second near-infrared photothermal materials for combinational nanotheranostics. *Chem Soc Rev* 2021;**50**:1111−37.
56. Li HD, Kim HJ, Xu F, Han JJ, Yao QC, Wang JY, et al. Activity-based NIR fluorescent probes based on the versatile hemicyanine scaffold: design strategy, biomedical applications, and outlook. *Chem Soc Rev* 2022;**51**:1795−835.
57. Jiang YY, Huang JG, Xu C, Pu KY. Activatable polymer nanoagonist for second near-infrared photothermal immunotherapy of cancer. *Nat Commun* 2021;**12**:742.
58. Wu X, Jiang YY, Rommelfanger NJ, Yang F, Zhou Q, Yin RK, et al. Tether-free photothermal deep-brain stimulation in freely behaving mice *via* wide-field illumination in the near-infrared-II window. *Nat Biomed Eng* 2022;**6**:754−70.
59. Xu MK, Zhang C, He SS, Xu C, Wei X, Pu KY. Activatable immunoprotease nanorestimulator for second near-infrared photothermal immunotherapy of cancer. *ACS Nano* 2023;**17**:8183−94.
60. Li JG, Kang MM, Zhang ZJ, Li X, Xu WL, Wang D, et al. Synchronously manipulating absorption and extinction coefficient of semiconducting polymers *via* precise dual-acceptor engineering for NIR-II excited photothermal theranostics. *Angew Chem Int Ed* 2023; **135**:e202301617.
61. Qin Y, Chen XH, Gui YX, Wang H, Tang BZ, Wang D. Self-assembled metallacage with second near-infrared aggregation-induced emission for enhanced multimodal theranostics. *J Am Chem Soc* 2022; **144**:12825−33.
62. Zhang ZJ, Xu WH, Kang MM, Wen HF, Guo H, Zhang PF, et al. An all-round athlete on the track of phototheranostics: subtly regulating the balance between radiative and nonradiative decays for multimodal imaging-guided synergistic therapy. *Adv Mater* 2020;**32**:e2003210.
63. Li SL, Deng QY, Zhang YC, Li XZ, Wen GH, Cui X, et al. Rational design of conjugated small molecules for superior photothermal theranostics in the NIR-II biowindow. *Adv Mater* 2020;**32**:e2001146.
64. Feng G, Zhang GQ, Ding D. Design of superior phototheranostic agents guided by Jablonski diagrams. *Chem Soc Rev* 2020;**49**: 8179−234.